NACA ASE FILE

RESEARCH MEMORANDUM

INVESTIGATION AT HIGH SUBSONIC SPEEDS OF THE

STATIC LATERAL AND DIRECTIONAL STABILITY AND TAIL-LOADS

CHARACTERISTICS OF A MODEL HAVING A HIGHLY TAPERED SWEPT

WING OF ASPECT RATIO 3 AND TWO HORIZONTAL-TAIL FOSITIONS

By Albert G. Few, Jr.

Langley Aeronautical Laboratory
Langley Field, Va.

CLASSIFIED DOCUMENT

This material contains information affecting the National Defense of the United States within the most the espionage laws, Title 18, U.S.C., Secs. 793 and 794, the transmission or revelation of which if manner to an unauthorized person is prohibited by law.

NATIONAL ADVISORY COMMITTEE FOR AERONAUTICS

WASHINGTON

September 11, 1956

CONFIDENTIAL

NATIONAL ADVISORY COMMITTEE FOR AERONAUTICS RESEARCH MEMORANDUM

INVESTIGATION AT HIGH SUBSONIC SPEEDS OF THE

STATIC LATERAL AND DIRECTIONAL STABILITY AND TAIL-LOADS

CHARACTERISTICS OF A MODEL HAVING A HIGHLY TAPERED SWEPT

WING OF ASPECT RATIO 3 AND TWO HORIZONTAL-TAIL POSITIONS

By Albert G. Few, Jr.

SUMMARY

An investigation has been made in the Langley high-speed 7- by 10-foot tunnel of the static lateral and directional stability and some tail-loads characteristics of a model having a highly tapered swept wing and two horizontal-tail positions. The wing was of aspect ratio 3, taper ratio 0.14, and had NACA 65A006 airfoil sections parallel to the plane of symmetry. Tests were made both with the horizontal tail located at the tip of the swept vertical tail and with the horizontal tail located in the wing-chord plane extended. Test Mach numbers ranged from 0.80 to 0.92, which corresponds to a Reynolds number range from approximately 4.0×10^6 to 4.2×10^6 based on the wing mean aerodynamic chord.

Effective vertical-tail centers of pressure extracted from tail contributions to the stability derivatives were considerably different from the centers of pressure obtained from the tail-loads measurements, particularly at high angles of attack. The differences appeared to result primarily from loads induced on the wing and fuselage by the vertical tail. The high horizontal tail raises the effective center of pressure of the vertical tail; however, this results almost entirely from the horizontal-tail rolling-moment contribution to the vertical-tail root bending moment and, to a very small extent, from changes in vertical-tail loading. In an angle-of-attack range from 0° to approximately 15°, the normal force measured on the exposed vertical-tail assembly generally was from 80 to 90 percent of the total tail contribution to the lateral force of the complete model.

Addition of the wing generally produced an adverse effect on directional stability at high angles of attack for both the high and the low horizontal-tail positions. The low horizontal tail produced relatively small effects on directional stability throughout the range of test variables. The high horizontal tail generally had a favorable effect on directional stability; however, for the test configuration an unfavorable effect was indicated at low angles of attack for Mach numbers of 0.90 and 0.92.

INTRODUCTION

The design trend of high-speed airplanes has resulted in certain combinations of airplane aerodynamic and mass characteristics which have sometimes allowed some of these airplanes to attain attitudes in certain maneuvers which have subjected the rearward fuselage and tail surfaces to dangerously high loads. It therefore has become important that the airplane designer be furnished with more information as a basis for structural design and also to provide more information required for improved procedures for estimating the tail contribution to the lateral and directional stability. (See refs. 1 to 4.) Existing procedures for estimating the load on some tail configurations at low angles of attack and at subsonic and supersonic speeds are pointed out in reference 2. Methods for calculating these loads at low angles of attack are not necessarily valid for calculating the loads at higher angles of attack, since the vertical tail may be operating in a highly disturbed flow field from the wing and fuselage. Therefore, any calculations should be based on an understanding of the strength and position of the wing and fuselage flow field at the tail. Reference 5 presents some theoretical and experimental results of tail flow-field studies and reference 2 outlines several procedures that may be used in order to determine the strength and position of the trailing vortices from the wing and fuselage.

The purpose of the present investigation was to determine experimentally at high subsonic speeds the static lateral and directional stability characteristics and the static tail loads in sideslip on a model having a highly tapered swept wing and the horizontal tail in either of two positions. The wing was of aspect ratio 3, taper ratio 0.14, and had NACA 65AOO6 airfoil sections. The leading edges of the wing and of the delta horizontal tail were swept back 45°.

Tests were made both with the horizontal tail located at the tip of the swept vertical tail and with the tail on the center line of the fuse-lage. In addition to tests of the complete model, breakdown tests were made in order to determine the contribution of the tail surfaces to static lateral and directional stability and tail-loads characteristics of the model with and without the wing. Test Mach numbers ranged from 0.80 to 0.92 with corresponding Reynolds numbers ranging from about 4.0×10^6 to 4.2×10^6 based on the wing mean aerodynamic chord. For some tests, the model angle of attack was varied from -2° to approximately 23° at sideslip angles of 4° and 4° . In another series of tests the model sideslip angle was varied from 4° to approximately 12° at several selected angles of attack.

Results presenting the static longitudinal stability and the rollingstability derivatives of the model are given in references 6 and 7, respectively.

COEFFICIENTS AND SYMBOLS

The overall force and moment coefficients are presented with respect to a stability-axis system, whereas the basic tail-load coefficients, unless otherwise noted, are presented with respect to axes fixed relative to the model (body axes). Figure 1 shows the system of axes used with arrows indicating positive values of forces and moments.

c_{L}	lift coefficient, Lift qS								
c _D '	drag coefficient, $\frac{\text{Drag}}{\text{qS}}$								
C_{m}	pitching-moment coefficient, Pitching moment qSc								
C _{l,s}	rolling-moment coefficient, Rolling moment qSb								
Cn,s	yawing-moment coefficient, Yawing moment qSb								
C _{Y,s}	lateral-force coefficient, <u>Lateral force</u> qS								
$^{\mathrm{C}}\mathrm{B}_{\mathrm{V}}$	vertical-tail root-bending-moment coefficient (vertical-tail root chord 0.154 ft above fuselage center line), Vertical-tail root bending moment qSVbV								
c_{n_V}	vertical-tail yawing-moment coefficient (referenced to $\bar{c}_V/_4$), $\underline{\text{Vertical-tail yawing moment}}_{qS_V\bar{c}_V}$								
$c^{M\Lambda}$	vertical-tail normal-force coefficient, <u>Vertical-tail normal force</u> qS _V								
c _{lh}	horizontal-tail rolling-moment coefficient (about the point of attachment to vertical tail), Horizontal-tail rolling moment qShbh								

- horizontal-tail length, distance from quarter-chord of wing mean aerodynamic chord to quarter-chord of horizontal-tail mean aerodynamic chord, measured parallel to fuselage center line, ft
- $l_{
 m V}$ vertical-tail length, distance from quarter-chord of wing mean aerodynamic chord to quarter chord of vertical-tail mean aerodynamic chord, measured parallel to fuselage center line, ft
- q dynamic pressure, $\frac{\rho_{V_0}^2}{2}$, lb/sq ft
- ρ mass density of air, slugs/cu ft
- $V_{\rm O}$ free-stream velocity, ft/sec
- M Mach number
- S wing area, sq ft
- S_V approximate exposed vertical-tail area, sq ft (based on vertical-tail root-chord length of 0.912 ft which is 0.154 ft above fuselage center line)
- Sh horizontal-tail area, sq ft
- c local wing chord parallel to plane of symmetry
- \bar{c} wing mean aerodynamic chord, $\frac{2}{\bar{S}} \int_0^{b/2} c^2 dy$, ft
- \bar{c}_{V} vertical-tail mean aerodynamic chord, ft
- ch horizontal-tail mean aerodynamic chord, ft
- b wing span, ft
- by exposed vertical-tail span, ft
- bh horizontal-tail span, ft
- x distance from leading edge of vertical-tail mean aerodynamic chord to center of load, ft

y spanwise distance from plane of model symmetry, ft

distance from vertical-tail root chord to center of load (vertical-tail root chord 0.154 ft above fuselage center line), ft

α angle of attack, deg

it horizontal-tail incidence angle, deg

β angle of sideslip, deg

A aspect ratio, b^2/S

A_e effective aspect ratio

$$C_{l_{\beta}} = \frac{\partial C_{l}}{\partial \beta}$$
, where $\partial \beta \approx 8^{\circ}$

$$c_{n_{\beta}} = \frac{\partial c_{n}}{\partial \beta}$$

$$C_{X^{B}} = \frac{9c_{X}}{9c_{X}}$$

$$C_{B_{V_{\beta}}} = \frac{\partial C_{B_{V}}}{\partial C_{B_{V}}}$$

$$C_{n_V} = \frac{\partial C_{n_V}}{\partial C}$$

$$C^{N\Lambda^{B}} = \frac{9B}{9C^{N\Lambda}}$$

$$C_{l_{h_{\beta}}} = \frac{\partial C_{l_{h}}}{\partial \beta}$$

chordwise location of vertical-tail effective center of pressure, 0.25 - $\frac{c_{n_{V_{\beta}}}}{c_{N_{V_{\beta}}}}$

spanwise location of vertical-tail effective center of pressure, $\frac{c_{B_{V_{\beta}}}}{c_{N_{V_{\beta}}}}$

 $\Delta^{CC}l_{eta}$ tail contribution to lateral- and directional-stability derivatives $\Delta^{CC}l_{eta}$

Model component designations:

W wing

F fuselage

V vertical tail

 H_{H} high horizontal tail (atop vertical tail)

H_{T.} low horizontal tail (in wing-chord plane extended)

MODEL AND APPARATUS

Details of the complete model as tested are given in figure 2 and are the same as those of the complete model with the highly tapered swept wing for which results are reported in references 6 and 7. A photograph of the model mounted on the sting-type support system is given as figure 3. The fuselage was of fineness ratio 10.94 and was constructed of aluminum. The physical characteristics of the fuselage, including afterbody ordinates, are given in figure 4. The wing was made of aluminum and had an aspect ratio of 3, a taper ratio of 0.14, a leading-edge sweep angle of 45°, and was mounted in the midposition on a circular fuselage. The wing airfoil section was NACA 65A006 parallel to the plane of symmetry. The triangular horizontal tail was made of steel

covered with plastic and Fiberglas and had an aspect ratio of 4 with NACA 65A006 airfoil sections in a free-stream direction. The model was tested with the horizontal tail (zero incidence angle) atop the vertical tail and in the wing-chord plane extended. The vertical tail was also made of steel covered with plastic and Fiberglas and had an aspect ratio of 1.02 based on an exposed area of the vertical tail of 0.454 square foot, a taper ratio of 0.46, and a quarter-chord sweep angle of 28°. Other details of the model are given in table I.

The model was tested on the sting-type support system shown in figure 3. With this support system the model can be remotely operated through an angle-of-attack range of approximately 26° in the plane of the vertical strut. By the utilization of couplings in the sting behind the model, the model can be rolled 90° so that either angle of attack or angle of sideslip can be the remotely controlled variable. With the wings horizontal, the couplings can be used to support the model at angles of sideslip of -4° and 4° , while the model is tested through the angle-of-attack range.

A six-component electrical strain-gage balance was mounted internally in the fuselage to measure the forces and moments acting on the model. Forces and moments acting on the vertical tail were measured by a three-component electrical strain-gage balance mounted internally in the fuselage at the base of the vertical tail. The high horizontal-tail rolling moment (about the point of attachment to the vertical tail) was measured by means of an electrical strain gage. No forces were measured on the horizontal tail in the low position. Some details of the three-component vertical-tail balance and the horizontal-tail rolling-moment gage installations are given in figure 2(c).

TESTS

The sting-supported model was tested in the Langley high-speed 7-by 10-foot tunnel through a Mach number range of 0.80 to 0.92, which corresponds to a Reynolds number range from approximately 4.0×10^6 to 4.2×10^6 , based on the wing mean aerodynamic chord.

The static lateral- and directional-stability derivatives were obtained at angles of sideslip of -4° and 4° through an angle-of-attack range which varied with loading conditions, the maximum range being from about -2° to 23°. In addition, tests were made at several selected angles of attack through a sideslip-angle range from about -4° to 12°.

The model forces and moments were measured by means of an electrical strain-gage balance mounted internally in the fuselage. Three components

of forces and moments were measured on the vertical tail; namely, normal force, yawing moment, and root bending moment. With the horizontal tail mounted in the high position, measurements of the rolling moment of the horizontal tail about its juncture with the vertical tail also were made.

A small gap existed between the juncture of the vertical tail and fuselage and was closed with a sponge seal. Some model load tests were made both with a sponge and with a solid seal to determine leakage effects.

CORRECTIONS

Jet-boundary corrections to the angle of attack were applied in accordance with reference 8. The jet-boundary corrections to the lateral force, yawing moment, and rolling moment were considered negligible and therefore were not applied. From past experience, it was found that tares due to sting support were negligible; therefore, these values were not applied. Blockage corrections were applied to the data by the method outlined in reference 9.

The angle of attack and angle of sideslip have been corrected for deflection of the sting support and balance system under load. No attempt has been made to correct the data for aeroelastic distortion of the model; however, based on past experience, it is believed these corrections are negligible.

RESULTS AND DISCUSSION

Presentation of Results

Basic model data: $C_{T} \text{ against } \alpha \dots \dots \dots \dots \dots$	Figure 5
$C_{l,s}$, $C_{n,s}$, $C_{Y,s}$ against β	6 to 9
$C_{l_{\beta}}$, $C_{n_{\beta}}$, $C_{Y_{\beta}}$ against α	and ll
Basic tail loads data:	
CBV against CNV	12
$\mathtt{C}_{\mathtt{n}_{f V}}$ against $\mathtt{C}_{\mathtt{N}_{f V}}$	13
$\mathtt{C}_{ ext{N}_{ ext{V}}}$ against eta	14
C_{lh} against β	15
$c_{\mathrm{B_V}}$, $c_{\mathrm{n_V}}$, $c_{\mathrm{N_V}}$ against β	16
$c_{B_{V_{\beta}}}$, $c_{n_{V_{\beta}}}$, $c_{N_{V_{\beta}}}$, $c_{l_{h_{\beta}}}$ against α	17

CONFIDENTIAL

Data related to analysis of results:	Figure
$\Delta C_{Y_{\beta}}$, $\Delta C_{n_{\beta}}$, $\Delta C_{l_{\beta}}$ against α	18
∂C _N ,	
$\frac{\partial C_{N_V}}{\partial \beta}$ against M	19
OCN,	
$\frac{\partial C_{N_V}}{\partial \beta}$ against α	20 and 21
$\left(\frac{A_e}{A}\right)_V$ against M	22
$\frac{Z}{b_V}$, $\frac{X}{\bar{c}_V}$ against α	23 to 25

The basic model data (figs. 5 to 11) are presented about a stability system of axes as shown in figure 1 and the coefficients have been based on the model wing area, span, and mean aerodynamic chord with moment reference at the quarter chord of the wing mean aerodynamic chord. The static lateral— and directional—stability derivatives (figs. 10 and 11) were obtained from tests at angles of sideslip of -4° and 4° through the angle-of-attack range; however, sideslip tests (in a range from -4° to approximately 12°) were made at several selected angles of attack for several model configurations (figs. 6 to 9).

The basic vertical-tail loads data and the rolling-moment coefficients (figs. 12 to 17) of the high horizontal tail about the point of attachment to the vertical tail are based on the area, span, and mean aerodynamic chord of the vertical tail and the area and span of the horizontal tail as given in table I. These data are about a body system of axes fixed in the model as shown in figure 1. The vertical-tail area is an approximate exposed area and is defined as that area included above a root chord that is slightly inside the fuselage; however, it will be referred to hereafter as exposed area. The vertical-tail yawing-moment coefficients Cny are referenced about the quarter chord of the verticaltail mean aerodynamic chord and the vertical-tail root-bending-moment coefficients $C_{B_{\mathrm{W}}}$ are referenced about the vertical-tail root-chord line which is 0.154 foot above the fuselage center line. The vertical-tail derivatives $c_{B_{V_{\beta}}}$, $c_{n_{V_{\beta}}}$, and $c_{N_{V_{\beta}}}$ and the high-horizontal-tail derivwere obtained from angles of sideslip of -40 and 40 throughout the angle-of-attack range.

Static Lateral and Directional Stability

Effects of seal. The static lateral- and directional-stability derivatives presented in figure 10 were determined with the vertical-tail loads balance installed with a sponge sealed gap; therefore, it was thought advisable to determine whether the model characteristics were influenced by the sponge rubber seal that had been installed at the base of the vertical tail. In view of this, tests were made to obtain the stability characteristics of a fuselage vertical-tail configuration in which the sponge seal was replaced by a solid seal. A comparison of results with the sponge and solid seal (fig. 11) indicates that some leakage through the sponge seal may have occurred, since slight losses in the lateral- and directional-stability derivatives are noted especially at the higher angles of attack. (These differences at $\alpha=20^{\circ}$ represent approximately 8 and 4 percent of the measured $C_{\rm NV}$ and $C_{\rm nV}$, respec-

tively, and less than 1 percent of $C_{B_{V_{\beta}}}$. These differences, however,

are not expected to affect the validity of the comparisons which are made herein, since all the data (model loads and tail loads) were obtained simultaneously with the junctures sealed with sponge rubber.

Tail contribution. The vertical-tail contribution to the static lateral- and directional-stability derivatives and the effect of horizontal-tail position (wing on and wing off) on this contribution are presented in figure 18 for Mach numbers of 0.80 and 0.92. In this figure are included, for comparison, the vertical-tail contribution to the stability derivatives as determined from the data of model breakdown tests (presented in fig. 10) and the contribution as determined from measured tail-loads data (presented in fig. 17). The measured tail-loads data, however, have been based on the model wing geometry and are presented about the stability system of axes for the comparison shown in figure 18. The increment between the tail contribution as obtained from measured tail-loads data (solid curve) and that which was obtained from measured model-loads data (dashed curve) represents an interference or load induced by the vertical tail on the wing and the fuselage. This induced load generally increases the increments of $\Delta C_{\rm n}$ and $\Delta C_{\rm Y}$ at

least through a large part of the test angle-of-attack range; however, a decrease in the effective dihedral increment $\Delta C_{l_{\beta}}$ is noted which is

somewhat greater for the wing-on than for the wing-off configuration. At angles of attack below 15°, the measured vertical-tail normal force generally accounts for about 80 to 90 percent of the tail contribution to the lateral force $\Delta C_{Y_{\beta}}$ of the complete model.

From the standpoint of tail effectiveness, the vertical tail contributes a stabilizing increment to the directional stability $c_{n_{\rm g}}$

of the model throughout the angle-of-attack range as shown in figure 18; however, the stabilizing increment $\Delta C_{n_{\beta}}$ is greatly reduced at the higher angles of attack, as shown by data obtained at a Mach number of 0.80 and for the present wing-on configuration in which the wing is mounted in a midfuselage position. This reduction in $\Delta C_{n_{\beta}}$ at the higher angles of attack is somewhat more pronounced with the horizontal tail in the high position than for the low-tail or horizontal-tail-off configurations.

In general the end-plate effect provided by the high horizontal tail produces considerable increases in ΔC_{n_β} throughout the range of test angles of attack, especially at the lowest Mach number. This end-plate effect, of course, is also shown in figure 10(a) where increases in C_{n_β} for the complete model with the high horizontal tail are shown to exist at a Mach number of 0.80. At the higher Mach numbers (0.90 and 0.92) the favorable end-plate effect is lost and even becomes reversed at low angles of attack for the high-tail configurations tested. Results presented in reference 10 indicated that the loss in end-plate effect apparently resulted from a bad interference condition at the juncture of the horizontal and vertical tails. These adverse interference effects were reduced by moving the horizontal tail rearward so that its apex was approximately coincident with the leading edge of the vertical tail. This, however, caused some reduction in end-plate effect at the lower Mach numbers.

Vertical-Tail Loads

Mach number effects. The variation with Mach number of the vertical-tail normal force per degree of sideslip angle $\frac{\partial C_{N_V}}{\partial \beta}$ is presented in

figure 19. The values of $\frac{\partial c_{NV}}{\partial \beta}$ are almost identical when determined at $\beta=\pm 4^{\circ}$ from parameter tests or from sideslip tests at $\alpha=0^{\circ}$. The difference between the slopes measured near $\beta=0^{\circ}$ and those obtained from parameter tests indicates the presence of some nonlinearities in the normal-force curves for sideslip angles between -4° and 4° . Figure 14 presents results that also indicate these nonlinearities especially for the high horizontal-tail configuration. Since the following analysis is based on results obtained from the parameter tests ($\pm 4^{\circ}$ sideslip), it should be appreciated that the results may not truly represent the slopes at smaller sideslip angles. In general, the effect of Mach number on the vertical-tail normal force is small when the horizontal tail is located in the wing-chord plane extended; however, when the horizontal tail is located in the high position, appreciable reductions

in $\frac{\partial C_{N_V}}{\partial \beta}$ are evident at an angle of attack of 0° as Mach number increases. (See fig. 19.)

Comparison of total-tail contribution and load on exposed vertical tail .- The data presented in figure 20 include both the total-tail contribution and the load measured on the exposed vertical tail, both being based on exposed tail area. The total-tail contribution was determined from the differences between vertical-tail-on and tail-off tests which includes both the load carried on the exposed vertical tail and the load that the vertical tail induces on the fuselage. Differences are shown to exist between the total-tail contribution and the exposed tail load which indicate the load that is induced on the fuselage by the vertical tail and this load is referred to as the interference fuselage load in figure 20. For the wing-on configuration (fig. 20(a)) the fuselage load is slightly greater throughout the test angle-of-attack range when the horizontal tail is placed in the low position than for the horizontal tail in the high position or off. It will be noted that the induced fuselage load decreases more rapidly with angle of attack for the wing-off configuration than for the wing-on configuration and even changes sign at the higher angles of attack for the wing-off configuration. The delay in fuselage load reversal noted for the wing-on configuration is probably a result of wing-wake effects.

The total tail contribution and the load on the exposed vertical tail is considerably greater when the horizontal tail is placed in the high position for both the wing-on and wing-off configurations; however, reductions are evidenced with increased angle of attack with all horizontal-tail positions for the complete model configuration. The low

values of $\frac{\partial c_{N_V}}{\partial \beta}$ at the higher angles of attack for the complete model configuration (fig. 20(a)) do not necessarily indicate low overall tail

loads, as pointed out in reference 2, because this low value of $\frac{-v}{\partial \beta}$ is also indicative of low static-directional stability. Therefore, under the conditions of low static-directional stability (fig. 10) large angles of sideslip might be expected and, consequently, the tail loads at high angles of attack may be more critical than at the lower angles of attack.

Effect of horizontal-tail position on exposed vertical-tail load.—
In order to illustrate further some effects of horizontal-tail position on the exposed-vertical-tail load, some of the data from previous figures have been presented in figure 21 for a more direct comparison.
The horizontal tail in the wing-chord plane extended had little effect

on the exposed vertical-tail load throughout the test range of Mach number. At a Mach number of 0.80, the horizontal tail, when placed in the high position, produces an end-plate effect, or an increase in effective aspect ratio of the vertical tail, and thereby increases the verticaltail normal force through the angle-of-attack range. At a Mach number of 0.92, however, and in the vicinity of an angle of attack of 0°, a decrease in vertical-tail normal force exists, which is probably due to a bad interference condition at the juncture of the horizontal and vertical tails as discussed previously. Results of reference 10 at a Mach number of 0.90 have indicated that significant increases in the directional stability Cng, at or near an angle of attack of Oo, can be obtained simply by moving the high horizontal tail longitudinally with respect to the vertical tail. Therefore, these increases in $C_{n_{\beta}}$ would be expected to be associated with increases in the exposed vertical-tail load and center of pressure when the horizontal tail is in the high position.

The results presented in figure 22 are used to illustrate further how the vertical-tail effective aspect ratio is influenced by Mach number and horizontal-tail position. The values of the ratio of effective aspect ratio of the vertical tail to geometric aspect ratio $\frac{A_e}{A}$ were derived by using the experimental $\frac{\partial C_{N_V}}{\partial \beta}$ from theoretical expressions presented in reference 11. From these results presented in figure 22 (α = 0°), the end-plate effect provided by the horizontal tails is evident. The effective aspect ratio of the vertical tail for the low-tail and tail-off configurations is about constant throughout the range of Mach number; whereas, the high tail decreases the effective aspect ratio as Mach number increases.

Vertical-tail effective center of pressure. The vertical-tail spanwise center of pressure will be referred to as an effective center of pressure since it was derived by dividing the vertical-tail root bending moment per degree of sideslip by the vertical-tail normal force per degree of sideslip. For the comparisons presented in figure 23, the spanwise location of the effective center of pressure $\frac{Z}{b_V}$ also

includes the rolling moment and side force that the high horizontal tail imposes on the vertical tail. The effective center of pressure, exclusive of the horizontal-tail rolling-moment couple (horizontal-tail side force included), is only slightly affected by the high horizontal tail, and this effect is generally to shift the center of pressure outboard (toward tip of tail), especially near angle of attack of 0° and at a Mach number of 0.80. At a Mach number of 0.92, however, the center of pressure

shifts slightly inboard when the horizontal tail is placed in the high position. It would seem logical to assume that the greatest effect of the high horizontal tail on the vertical tail is to increase the normal-

force-curve slope of the vertical tail since large increases in $\frac{\delta c_{N_V}}{\delta \beta}$

are evident with only small changes in the center of pressure, especially at a Mach number of 0.80 (figs. 21 and 23). It will be noted that the rolling moment which the horizontal tail imposes on the vertical tail apparently is somewhat reduced with increased Mach number inasmuch as the increment between the curves of the location of the center of pressure with and without the horizontal-tail rolling-moment couple included are decreased at a Mach number of 0.92.

The variation of the chordwise location of the vertical-tail center of pressure $\frac{X}{\bar{c}_V}$ with angle of attack is included in figure 24 with the spanwise location of the center of pressure $\frac{Z}{b_V}$. The chordwise location of the effective center of pressure was obtained by dividing the vertical-tail yawing moment per degree of sideslip by the vertical-tail normal force per degree of sideslip. For the comparisons of horizontal-tail position shown in figure 24, the location of the vertical-tail spanwise center of pressure $\frac{Z}{b_V}$ for the configuration having the high horizontal tail includes the horizontal-tail rolling-moment couple that is added to the vertical-tail root bending moment. The chordwise location of the effective center of pressure $\frac{X}{\bar{c}_V}$ at a Mach number of 0.80 generally moves rearward with the addition of the horizontal tail and is farthest rearward when the tail is placed in the high position. However, $\frac{X}{\bar{c}_V}$ moves considerably forward at a Mach number of 0.92, especially at the lower angles of attack, with the horizontal tail in the high position.

moves considerably forward at a Mach number of 0.92, especially at the lower angles of attack, with the horizontal tail in the high position. In general the effective center of pressure of the vertical tail moves rearward and toward the tip with increasing angle of attack for all the horizontal-tail configurations, but is farthest rearward and toward the tip for the high-tail position, especially at a Mach number of 0.80. Similar results have been indicated in reference 12.

A comparison of the effective centers of pressure as determined from tail-loads measurements and as determined from tail-on and tail-off model stability derivatives is presented in figure 25. These comparisons are for the complete model having two horizontal-tail positions. It is evident that the center of pressure as extracted from the stability derivatives (dashed curve) is not at all in agreement with that which was determined from the tail-loads measurements. The center of pressure as

determined from stability derivatives is considerably rearward and toward the root, especially for a Mach number of 0.92. This difference may be attributed in part to a load induced on the wing and to a lesser extent on the fuselage by the vertical tail. (Compare ΔC_{lg} in

figs. 18(c) and 18(f).) Approximate unpublished calculations for this wing have been made based on tail pressure distribution, and these calculations would tend to verify the assumption that the vertical tail induces a load on the wing.

CONCLUSIONS

A wind-tunnel investigation at high subsonic speeds of the static lateral and directional stability and the tail-loads characteristics of a model having a highly tapered swept wing and two horizontal-tail positions indicate the following results:

- l. Effective vertical-tail centers of pressure derived from the tail contributions to the stability derivatives were considerably different from the centers of pressure obtained from tail-loads measurements, particularly at high angles of attack. The differences appeared to result primarily from loads induced on the wing and fuselage by the vertical tail.
- 2. Addition of a horizontal tail at the top of a vertical tail raises the effective center of pressure of the tail assembly; however, this results almost entirely from the horizontal-tail root bending moment and to a very small extent from changes in vertical-tail loading.
- 3. In the angle-of-attack range from 0° to approximately 15°, the normal force measured on the exposed tail assembly generally was from 80 to 90 percent of the tail contribution to the lateral force of the complete model.
- 4. Addition of the wing in a midfuselage position generally produced an adverse effect on the tail contribution to the directional stability at high angles of attack for any of the tail arrangements investigated.
- 5. Addition of a horizontal tail in a low position produced relatively small effects on directional stability throughout the range of test variables.
- 6. Addition of a horizontal tail at the top of the vertical tail generally increased the directional stability; however, for the test configuration, a decrease was indicated at low angles of attack for Mach numbers of 0.90 and 0.92.

Langley Aeronautical Laboratory,
National Advisory Committee for Aeronautics,
Langley Field, Va., May 11, 1956.

REFERENCES

- 1. Zimmerman, Charles H.: Recent Stability and Aerodynamic Problems and Their Implications as to Load Estimation. NACA RM L55Ella, 1955.
- 2. Kuhn, Richard E., Hallissy, Joseph M., Jr., and Stone, Ralph W., Jr.:
 A Discussion of Recent Wind-tunnel Studies Relating to the Problem
 of Estimating Vertical- and Horizontal-Tail Loads. NACA RM L55E16a,
 1955.
- 3. Malvestuto, Frank S., Jr., and Kuhn, Richard E.: Examination of Recent Lateral-Stability-Derivative Data. NACA RM 153108a, 1953.
- 4. Michael, William H., Jr.: Investigation of Mutual Interference Effects of Several Vertical-Tail—Fuselage Configurations in Sideslip. NACA TN 3135, 1954.
- 5. Malvestuto, Frank S., Jr., and Alford, William J., Jr.: Effects of Wing-Body Geometry on the Lateral-Flow Angularities at Subsonic Speeds. NACA RM L55L26a, 1956.
- 6. Few, Albert G., Jr.: Investigation at High Subsonic Speeds of the Static Longitudinal Stability Characteristics of a Model Having a Cropped-Delta and Unswept Wing Plan Forms and Several Tail Configurations. NACA RM L55123a, 1955.
- 7. Sleeman, William C., Jr., and Few, Albert G., Jr.: Experimental Investigation at High Subsonic Speed of the Rolling Stability Derivatives of a Complete Model Having a Clipped-Delta Wing and a High Horizontal Tail. NACA RM L55Kll, 1955.
- 8. Gillis, Clarence L., Polhamus, Edward C., and Gray, Joseph L., Jr.: Charts for Determining Jet-Boundary Corrections for Complete Models in 7- by 10-Foot Closed Rectangular Wind Tunnels. NACA WR L-123, 1945. (Formerly NACA ARR L5G31.)
- 9. Herriot, John G.: Blockage Corrections for Three-Dimensional-Flow Closed-Throat Wind Tunnels, With Consideration of the Effect of Compressibility. NACA Rep. 995, 1950. (Supersedes NACA RM A7B28.)
- 10. Polhamus, Edward C., and Hallissy, Joseph M., Jr.: Effect of Airplane Configuration on Static Stability at Subsonic and Transonic Speeds.

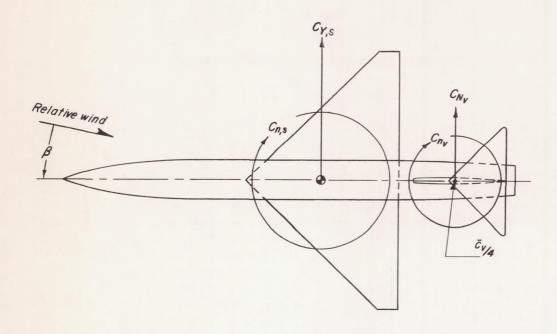
 NACA RM L56A09a, 1956.
- 11. Polhamus, Edward C., and Sleeman, William C., Jr.: The Rolling Moment Due to Sideslip of Swept Wings at Subsonic and Transonic Speeds. NACA RM L54LO1, 1955.

12. Hallissy, Joseph M., Jr.: Transonic Wind-Tunnel Measurements of Static Lateral and Directional Stability and Vertical-Tail Loads for a Model With a 45° Sweptback Wing. NACA RM L55L19, 1956.

TABLE I

PHYSICAL CHARACTERISTICS OF THE MODEL

Wing: Span, ft Root chord, Tip chord, f Mean aerodyn Area, sq ft Aspect ratio Taper ratio	ft . t . amic	chor	rd,	ft							 								2.572 1.500 0.214 1.018 2.20 3.00 0.143 36.85
Quarter-chor Airfoil sect																			
Horizontal tai Span, ft Root chord, Tip chord, f Mean aerodyn Area, sq ft Aspect ratio Taper ratio Quarter-chor Airfoil sect Vertical tail:	ft. t. amic	chords	rd, deg	ft							 							·	1.162 0.581 0 0.388 0.337 4.00 0 36.85 65A006
Span (measu	ed f	rom	root	c	ho:	rd),	ft	5		•	•	•	•	•	•	•		0.683
Root chord line), ft Tip chord,: Mean aerody Area, sq ft Aspect ratio Taper ratio Quarter-cho	rt amic	cho:	rd,	ft							 								0.912 0.420 0.696 0.454 1.02 0.46 28.00 65A006



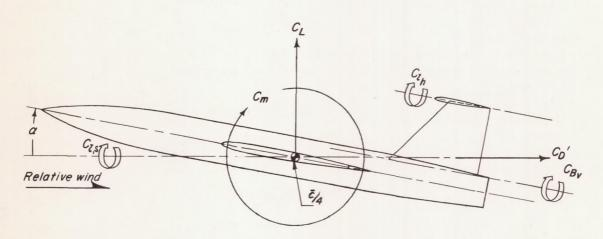
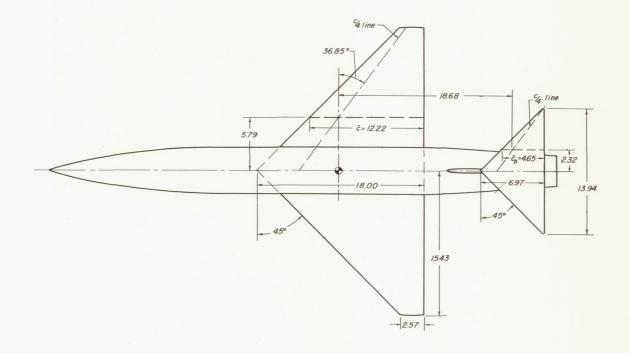
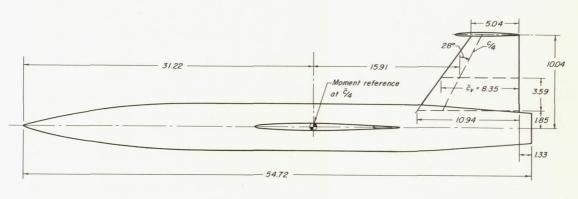


Figure 1.- System of axes used in presentation of data. Positive values of forces, moments, and angles are indicated by arrows.

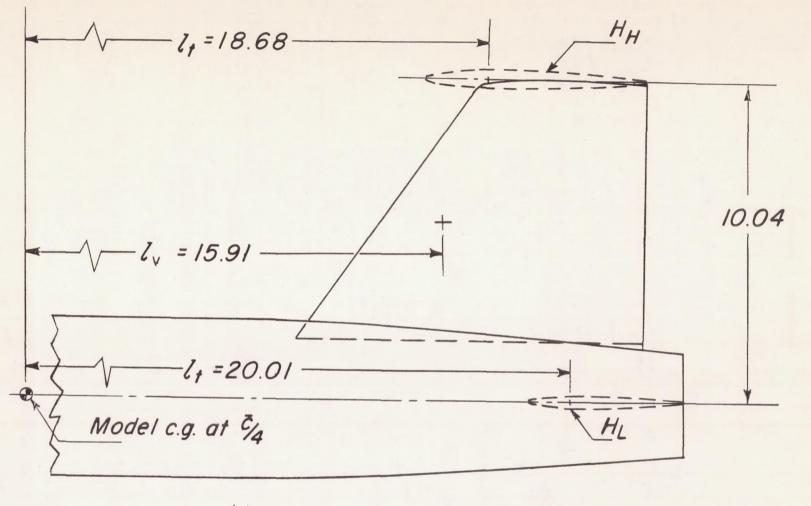




(a) Complete model.

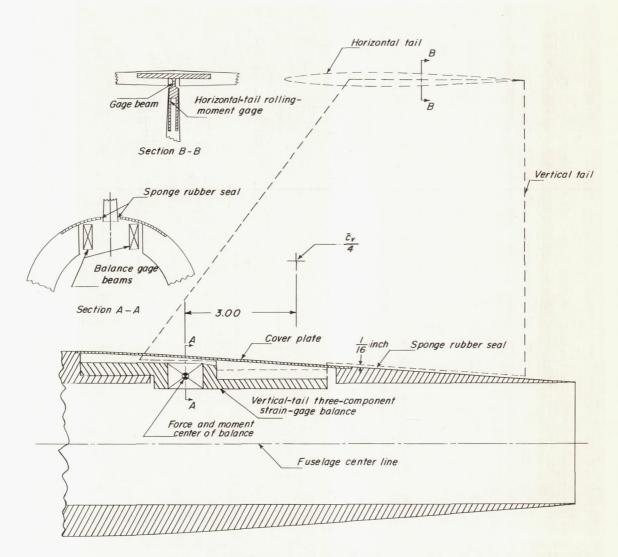
Figure 2.- Physical characteristics of test model. (All dimensions are in inches.)

CONFIDENTIAL



(b) Horizontal- and vertical-tail locations.

Figure 2.- Continued.



(c) Details of vertical- and horizontal-tail loads instrumentation.

Figure 2.- Concluded.

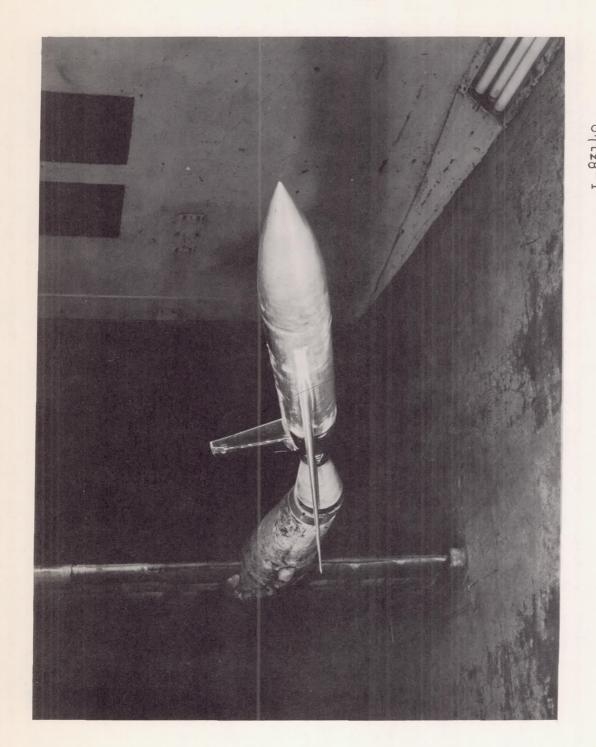
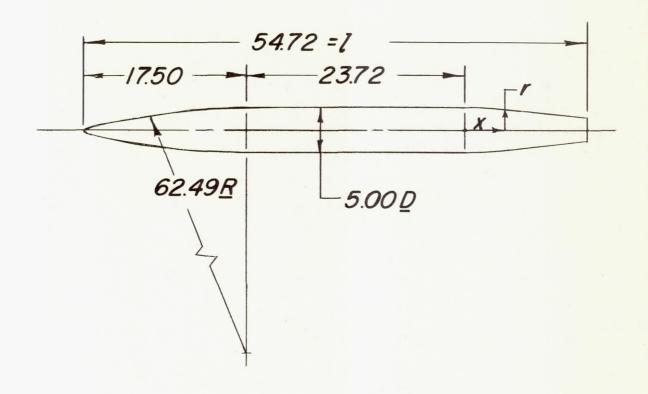


Figure 5.- Model mounted on the sting support system.



Afterbody Coordinates

X/Z	1/2
0	.0456
.0320	.0445
.0639	.0427
.1187	.0390
Straigh	ht-line
tap	er
.2460	.0301

Figure 4.- Fuselage dimensions in inches. Fineness ratio, 10.94.

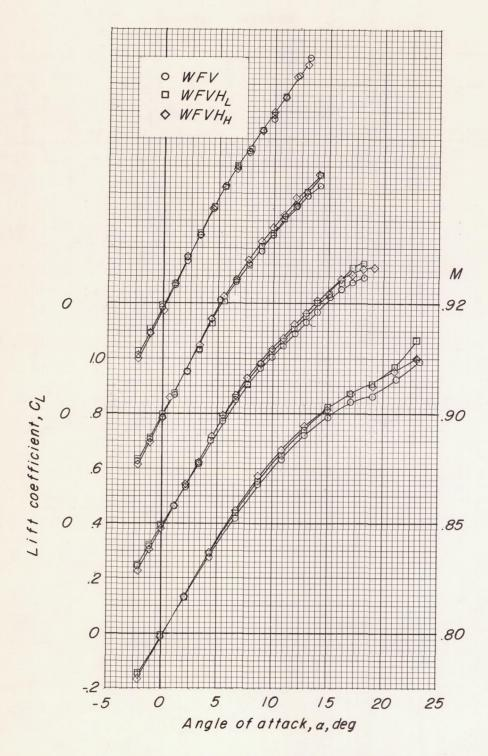


Figure 5.- Variation of model lift coefficient with angle of attack for both horizontal-tail positions. $i_t = 0^{\circ}$.

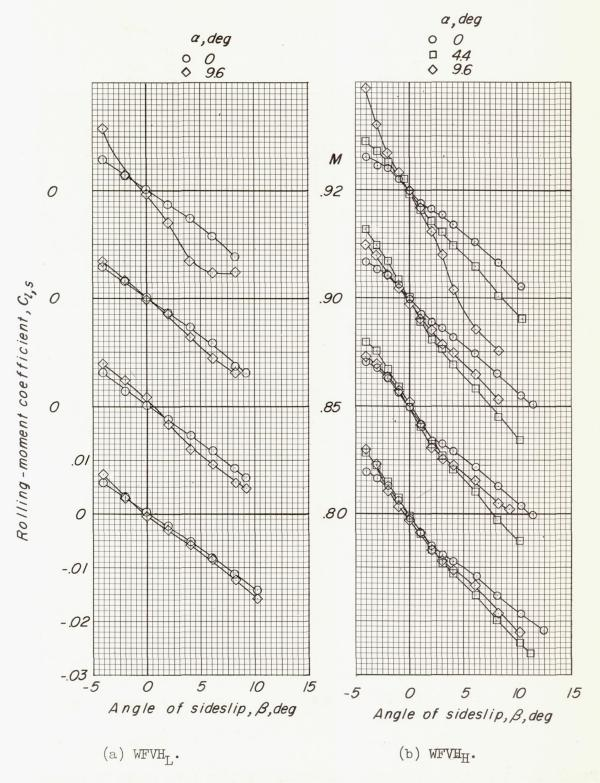


Figure 6.- Variation of rolling-moment coefficient with angle of sideslip.

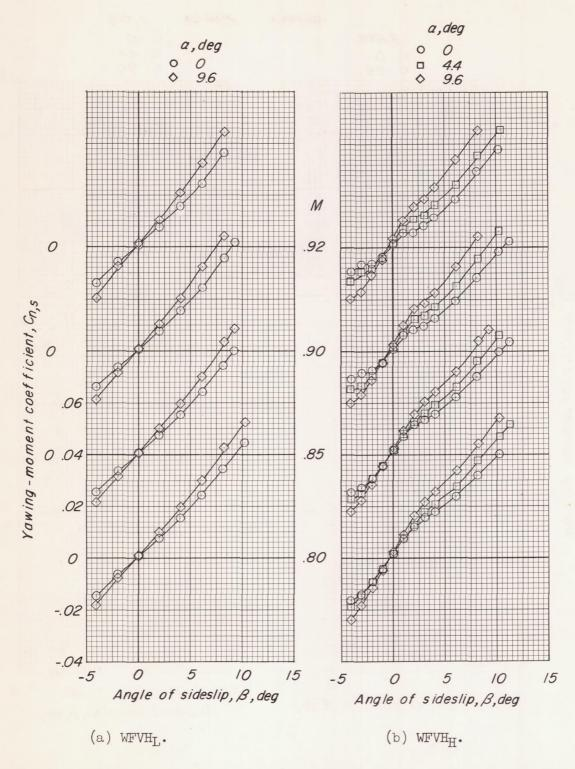


Figure 7.- Variation of yawing-moment coefficient with angle of sideslip.

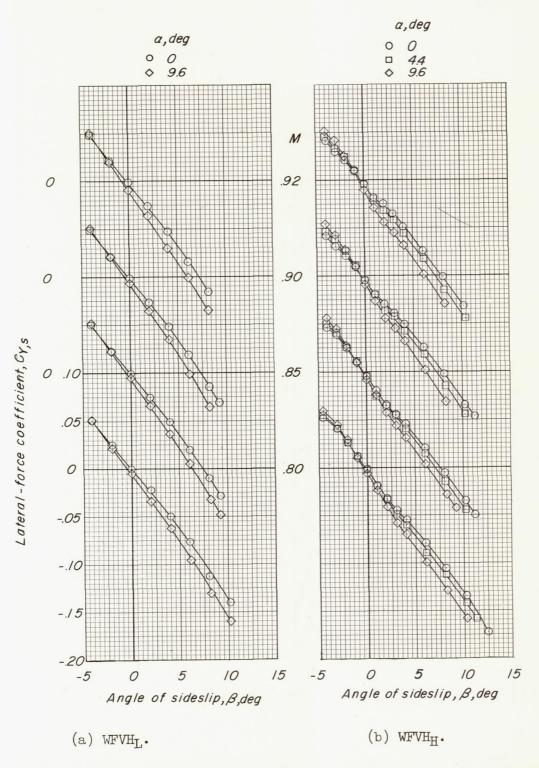


Figure 8.- Variation of the lateral-force coefficient with angle of sideslip.

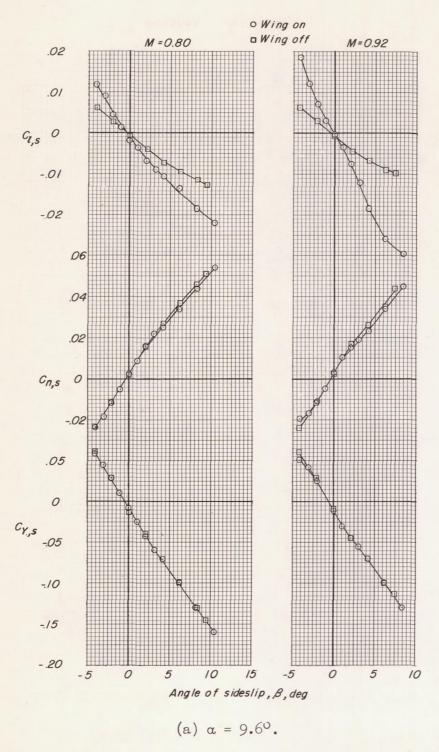


Figure 9.- Effect of the wing on lateral and directional stability characteristics of the model having a high horizontal tail.

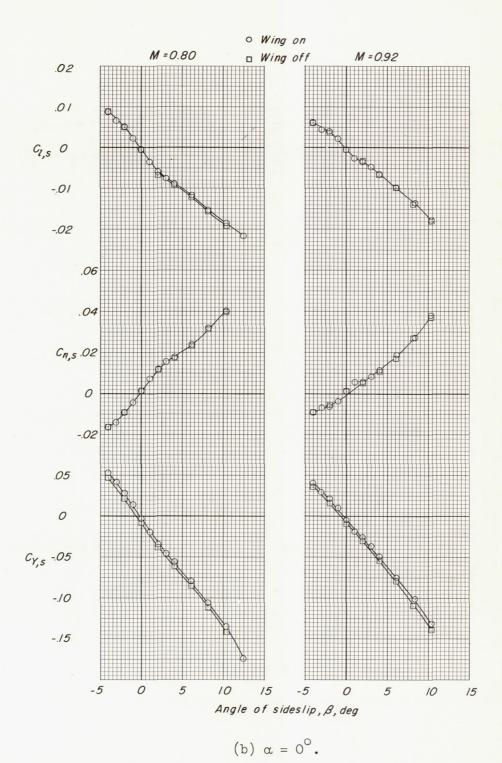


Figure 9.- Concluded.

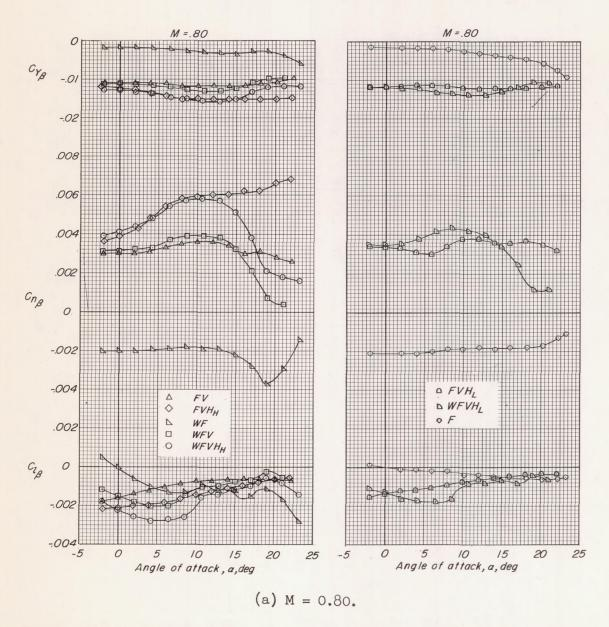
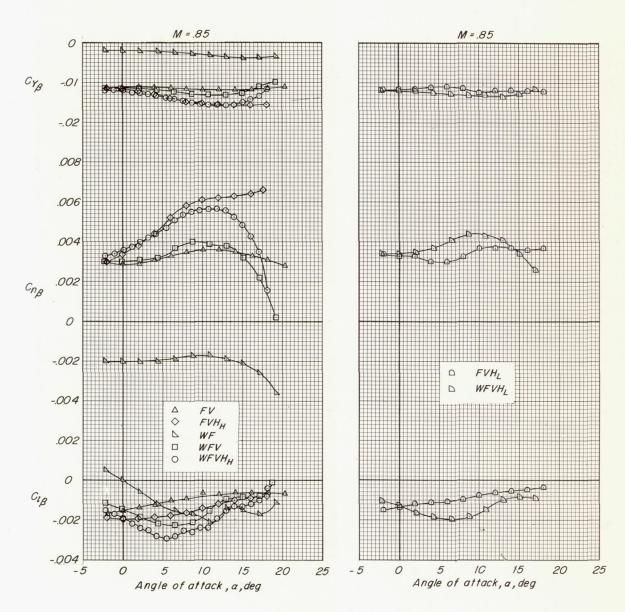
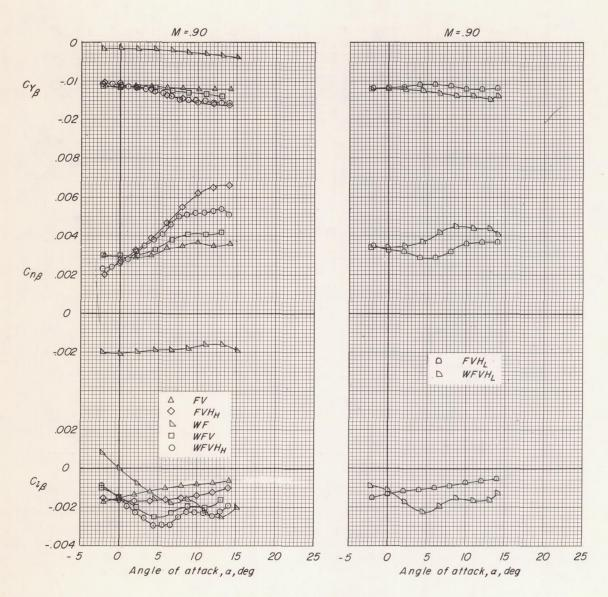


Figure 10.- Variation of lateral- and directional-stability derivatives with angle of attack.



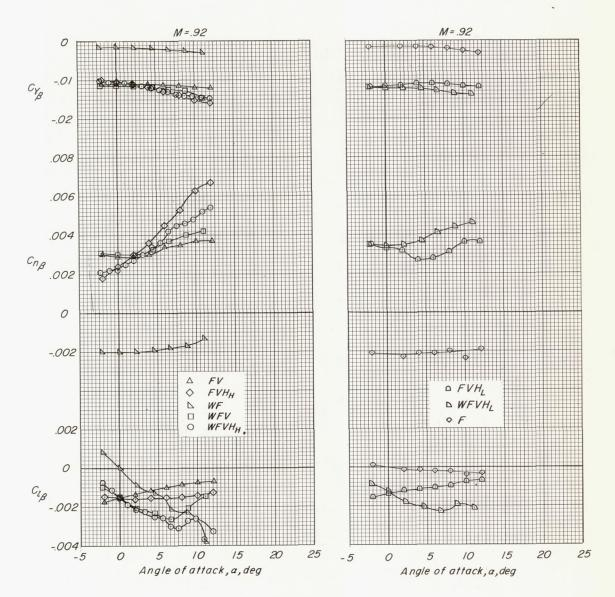
(b) M = 0.85.

Figure 10. - Continued.



(c) M = 0.90.

Figure 10. - Continued.



(d) M = 0.92.

Figure 10.- Concluded.

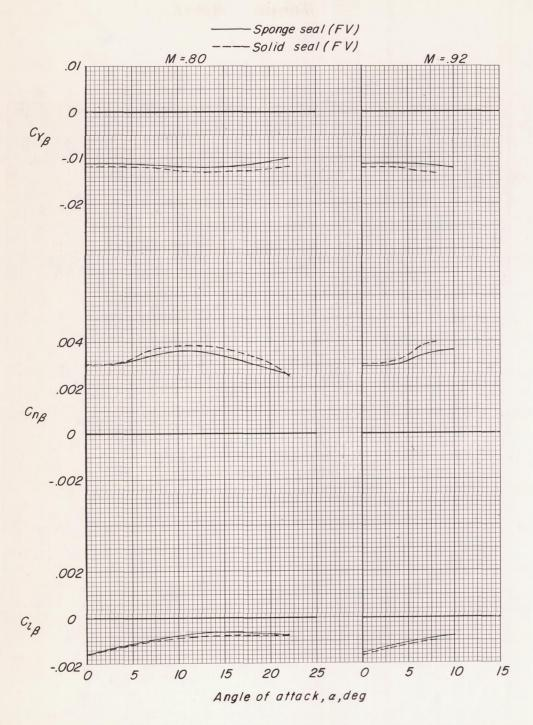


Figure 11.- Effect of a type of sealed fuselage—vertical-tail juncture on the static lateral- and directional-stability derivatives of the fuselage—vertical-tail configuration.

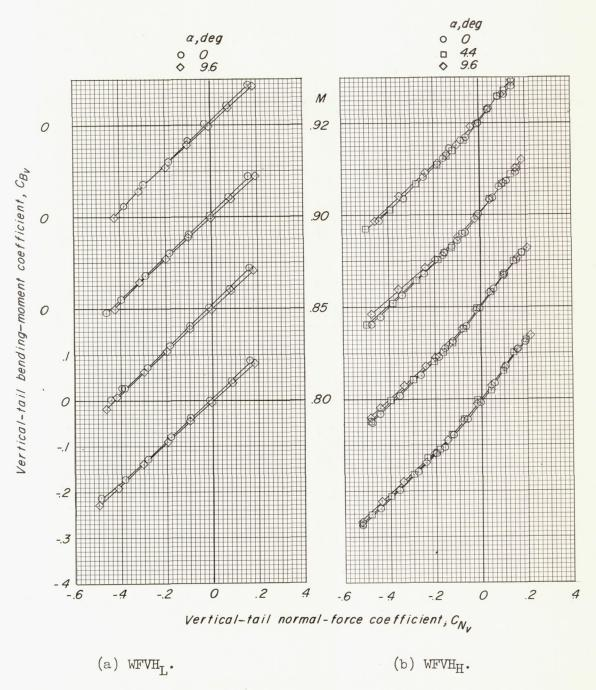


Figure 12.- Variation of the vertical-tail bending-moment coefficient with vertical-tail normal-force coefficient.

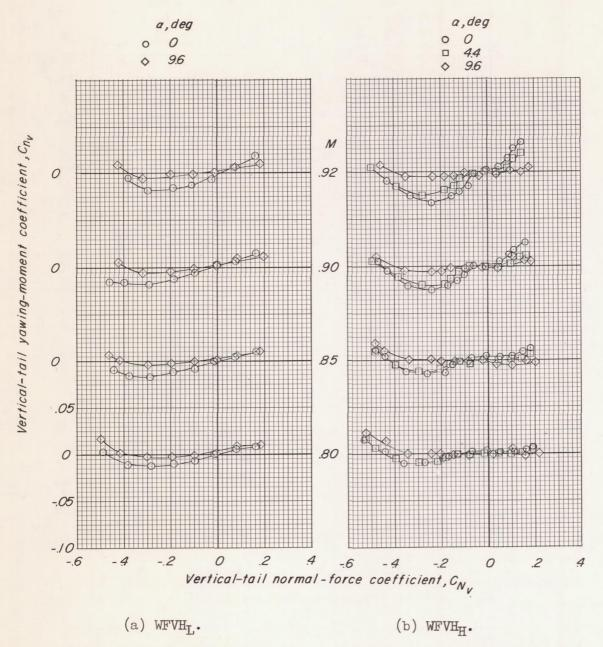


Figure 13.- Variation of vertical-tail yawing-moment coefficient with vertical-tail normal-force coefficient.

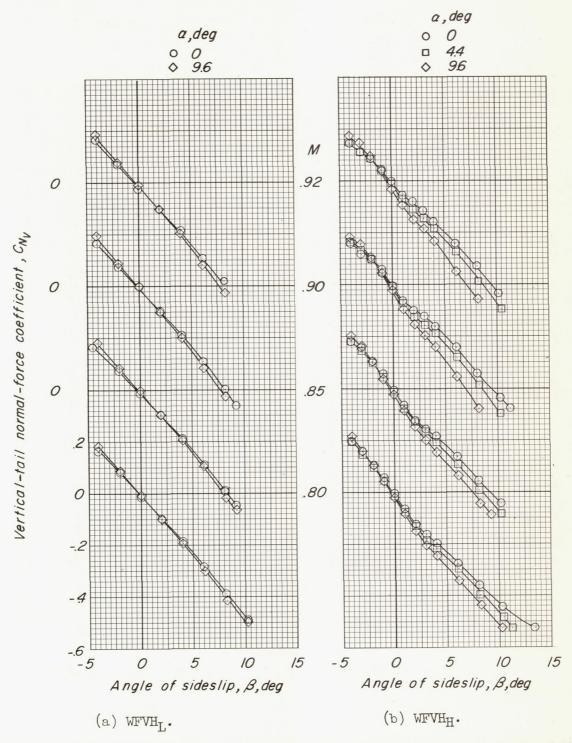


Figure 14.- Variation of vertical-tail normal-force coefficient with angle of sideslip.

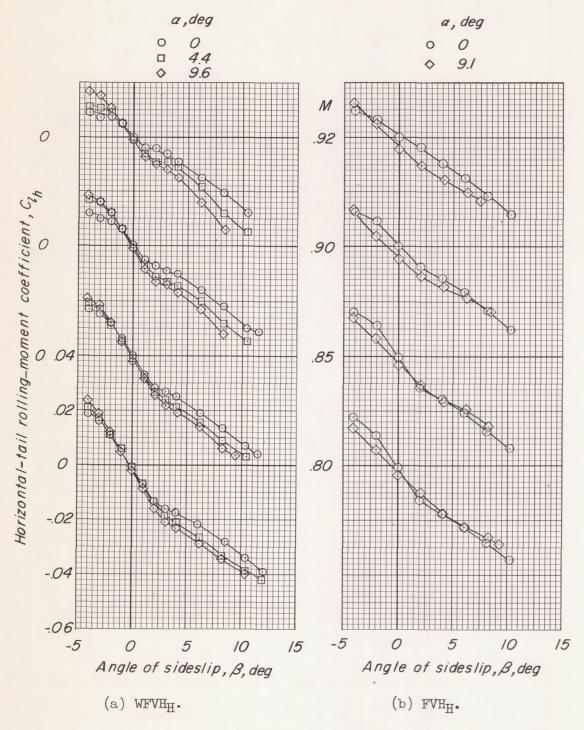


Figure 15.- Variation of high horizontal-tail rolling-moment coefficient with angle of sideslip.

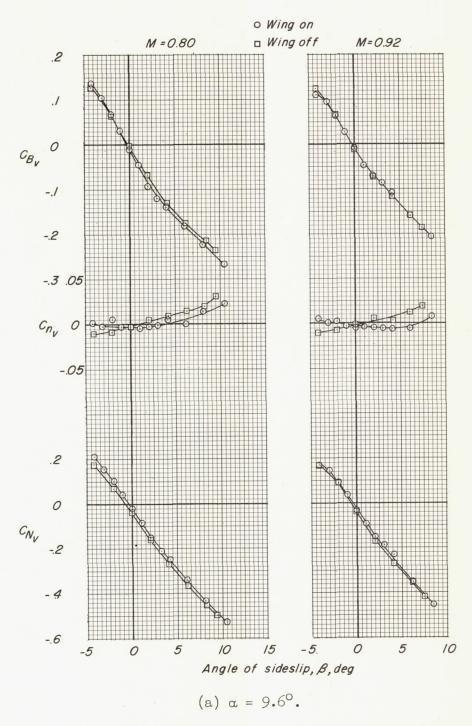
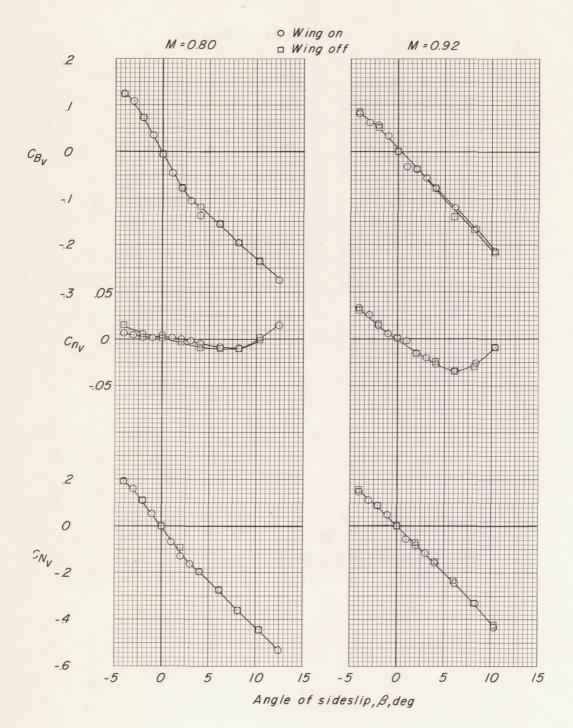
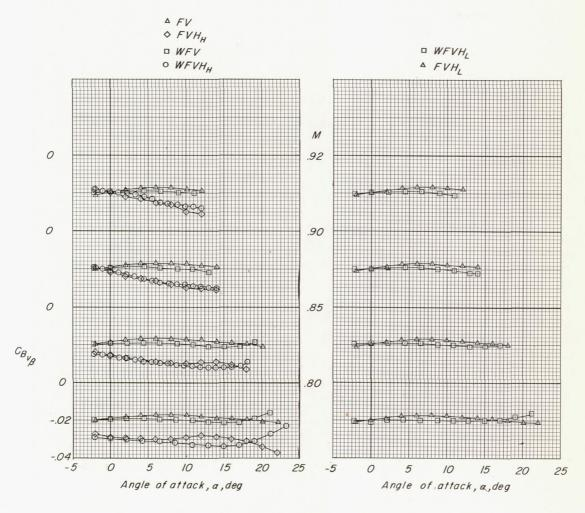


Figure 16.- Effect of the wing on vertical-tail bending, yawing, and normal-force coefficients with angle of sideslip for the model with the high horizontal tail.



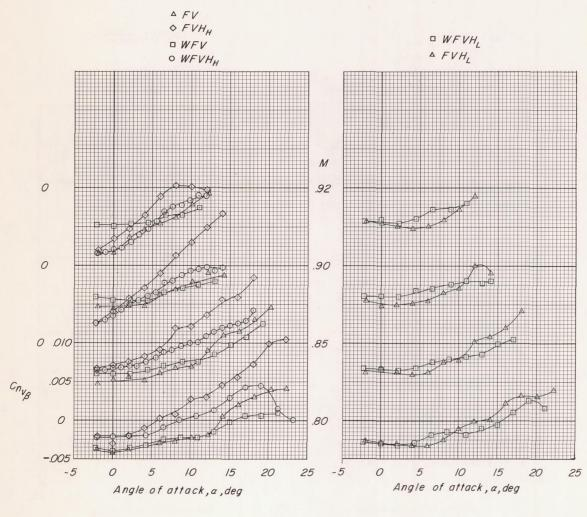
(b) $\alpha = 0^{\circ}$.

Figure 16.- Concluded.



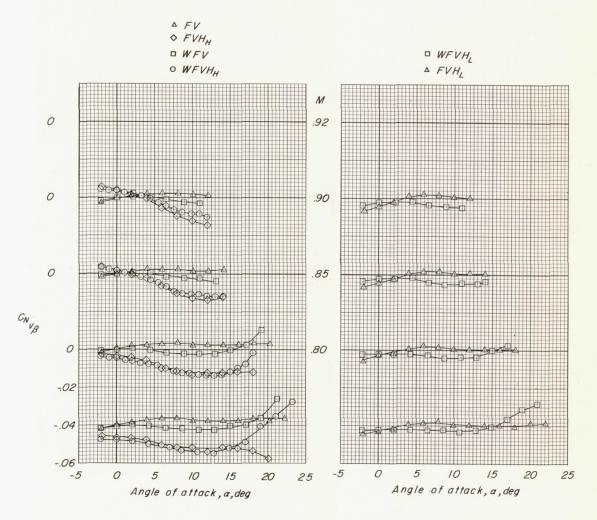
(a) $\text{C}_{\text{BV}_{\beta}}$ against $\alpha.$

Figure 17.- Variation of the vertical- and horizontal-tail derivatives with angle of attack.



(b) $\text{C}_{\text{n}\text{V}_{\beta}}$ against $\alpha.$

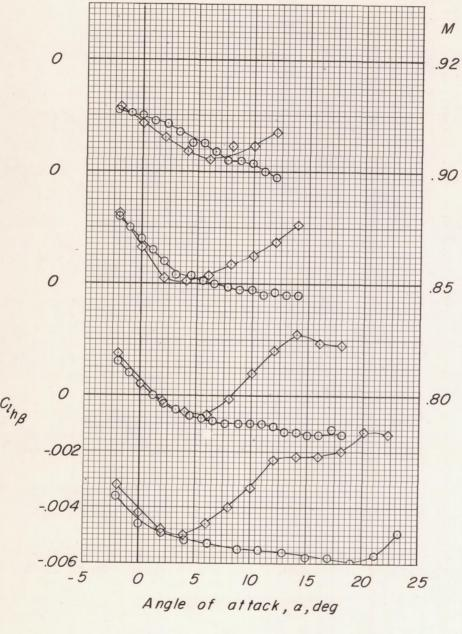
Figure 17.- Continued.



(c) CN_{V_β} against $\alpha.$

Figure 17.- Continued.





(d) $C_{lh_{\beta}}$ against α .

Figure 17.- Concluded.

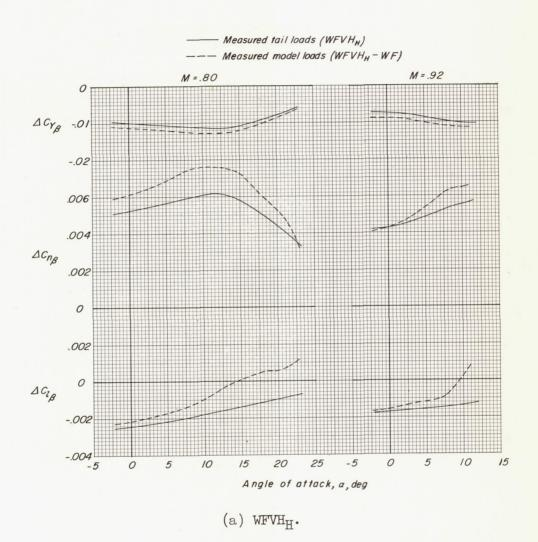
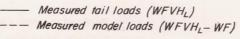
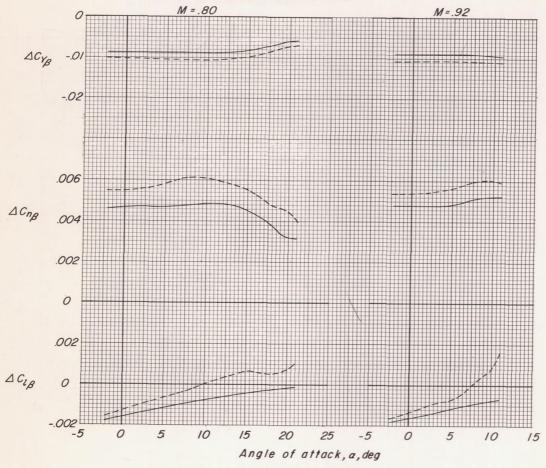


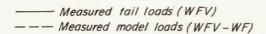
Figure 18.- Variation of the tail contribution to the static lateral- and directional-stability derivatives with angle of attack. (Stability axes.)

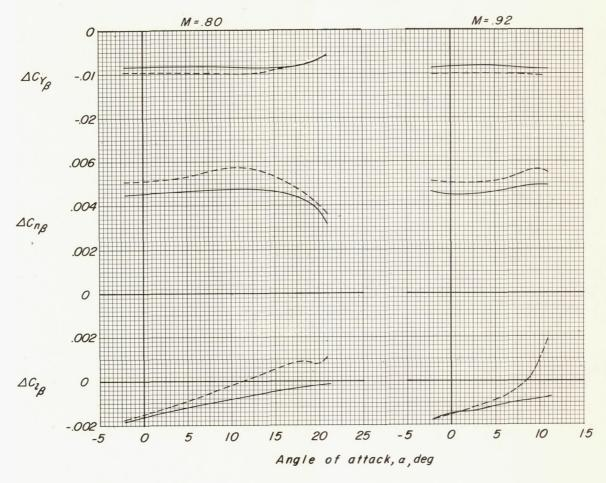




(b) WFVHL.

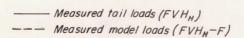
Figure 18.- Continued.

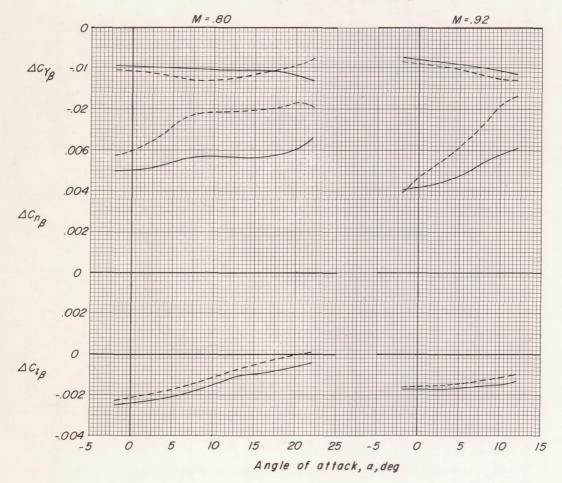




(c) WFV.

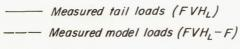
Figure 18.- Continued.

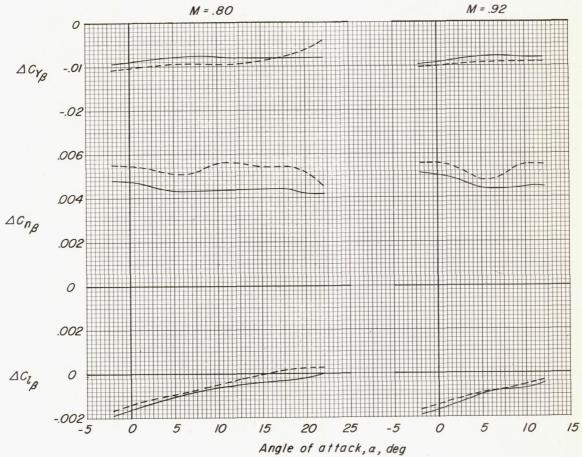




(d) FVHH.

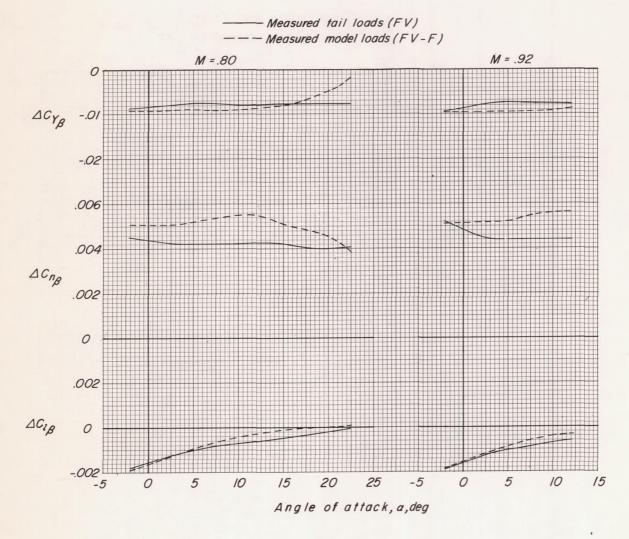
Figure 18.- Continued.





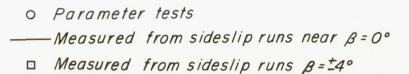
(e) FVH $_{\rm L}$.

Figure 18.- Continued.



(f) FV.

Figure 18.- Concluded.



Low tail

High tail

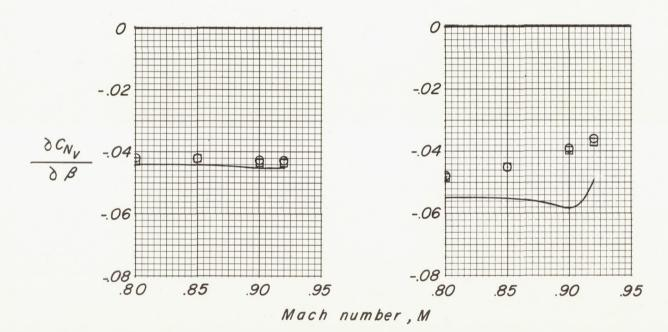


Figure 19.- Variation of the load on exposed vertical tail with Mach number. Wing on; $\alpha = 0^{\circ}$.

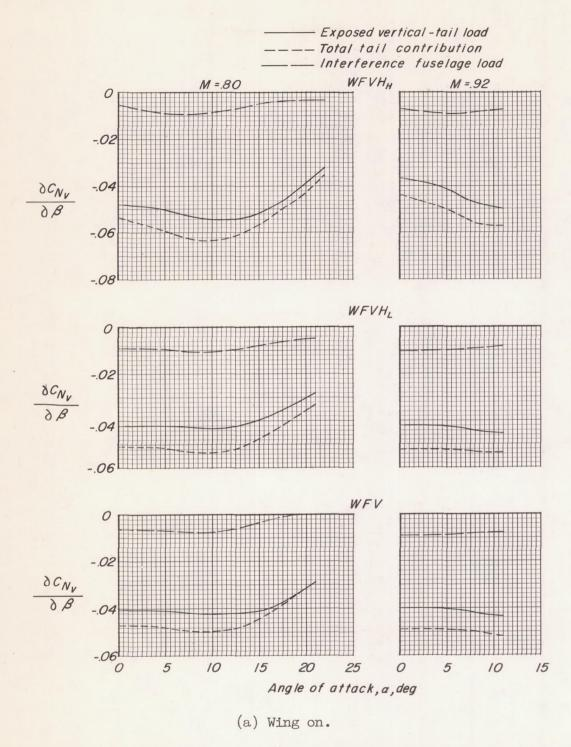
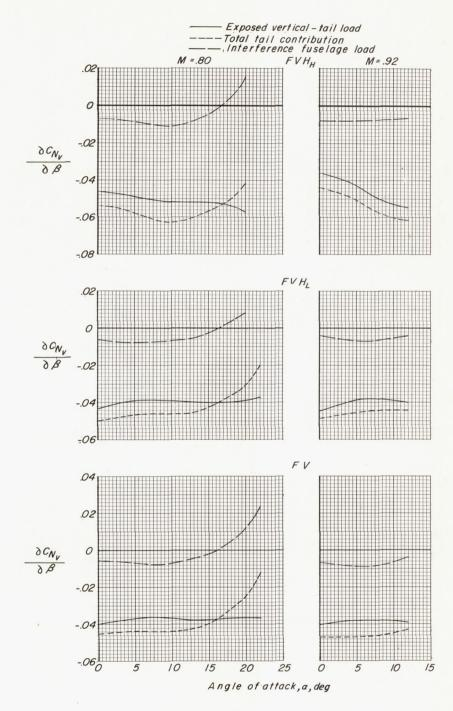


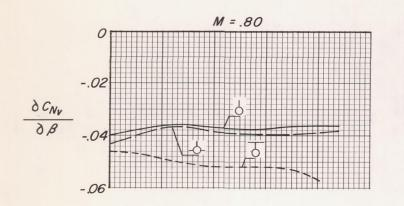
Figure 20.- Comparison of the total tail contribution and load on exposed vertical tail for several model configurations.

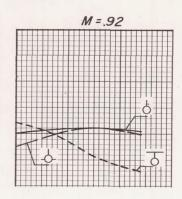


(b) Wing off.

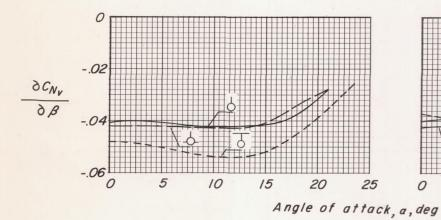
Figure 20.- Concluded.

Wing off





Wing on



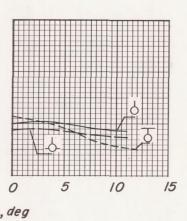


Figure 21.- Effect of horizontal-tail position on the exposed-vertical-tail load.

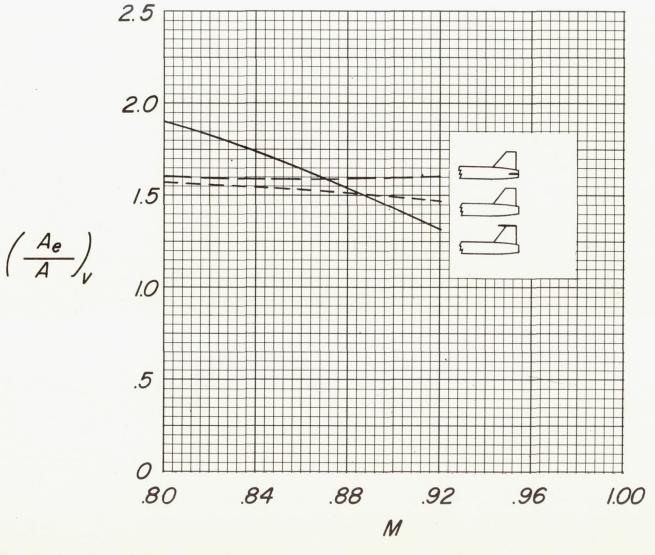
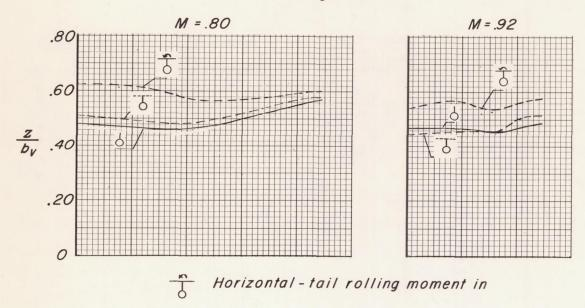


Figure 22.- Effect of horizontal-tail position on the vertical-tail effective aspect ratio. Wing on; $\alpha = 0^{\circ}$.





Horizontal - tail rolling moment out

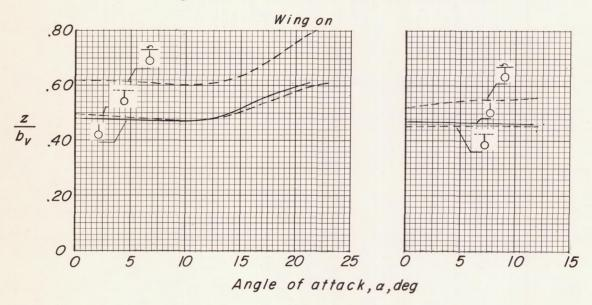


Figure 23.- Effect of a high horizontal tail on the variation of the effective center of pressure of the vertical tail with angle of attack.

58

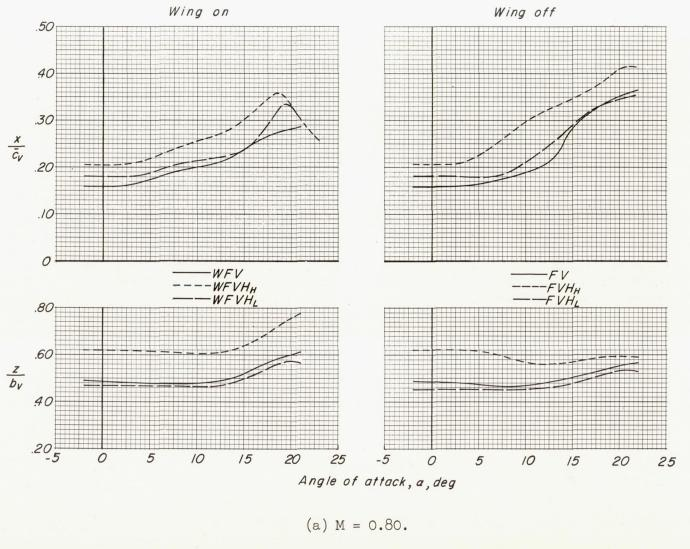
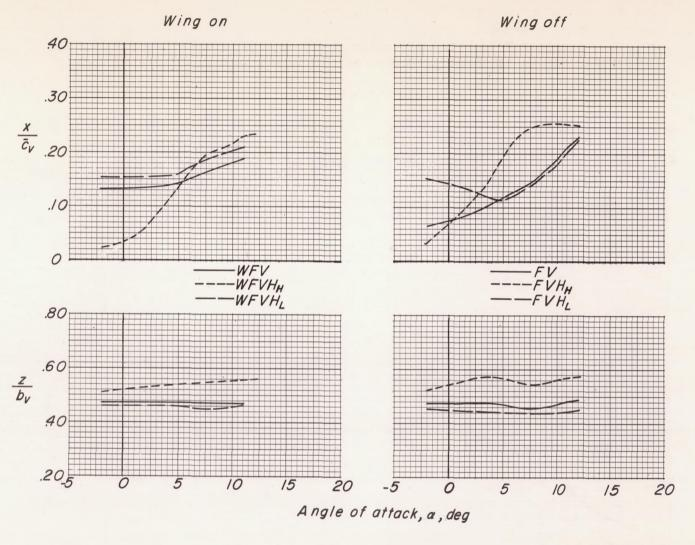


Figure 24.- Variation of the effective center of pressure of the vertical tail with angle of attack for several model configurations.



(b) M = 0.92.

Figure 24.- Concluded.

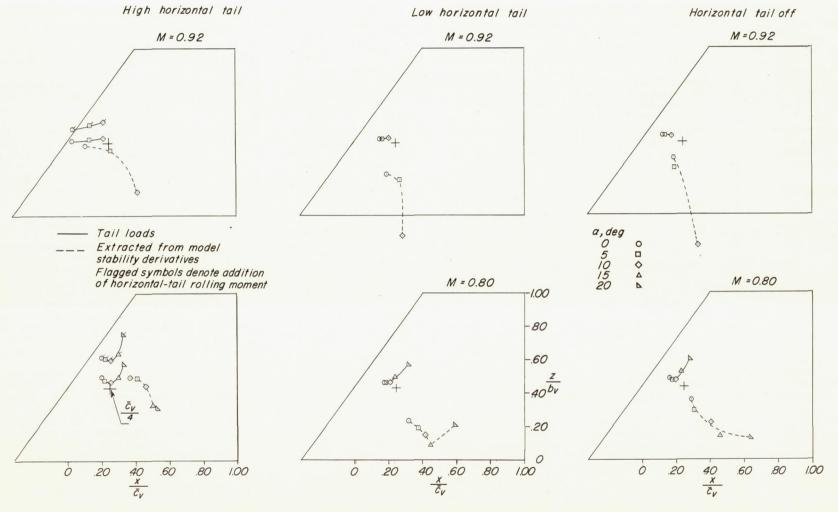


Figure 25.- Comparison of the effective centers of pressure as determined from tail-loads measurements and as determined from tail-on and tail-off stability derivatives. $b_{\rm V}$ = 8.19 inches; $\bar{c}_{\rm V}$ = 8.35 inches; wing on.

NACA - Langley Field, Va

CONFIDENTIAL